ORIGINAL PAPER

Experimental investigation of damage evolution and fracture mechanism in rocks with a single flaw under stepwise cyclic compression

Shuting Miao[1,2] · Peng-Zhi Pan[1,2] · Amin Hekmatnejad[3] · Yuxin Li[1,2]

Abstract

This study comprehensively investigates the damage and fracturing behaviors of sandstone specimens containing a single flaw under stepwise cyclic loading using digital image correlation (DIC) and acoustic emission (AE) techniques. The degradation of rocks is characterized by the evolution of residual strain, energy density, and cracking behaviors of flawed specimens while considering the effect of flaw inclination angle on the mechanical properties and fracturing behaviors of rocks. Experimental results reveal that residual strain gradually increases with an increasing number of cycles, and the increase in stress level induces a sudden rise in both elastic and dissipated energy density. The dissipation factor decreases initially and then reaches a constant value as the upper-stress limit increases. Moreover, the energy dissipation behavior becomes more consistent among the five cycles as the stress levels increase. Tensile wing cracks propagate stably during the stepwise cyclic loading process, accompanied by scattered low-amplitude AE events and a linear increase in cumulative AE counts. The analysis of normal and shear displacements indicates that wing cracks are primarily tensile, with significant normal opening displacements and negligible shear displacements. Horsetail cracks and anti-wing cracks initiate within fan-shaped strain zones of great size, driven by high compressive-shear stress, and rapidly propagate in the last one or two stress levels, leading to the detection of abundant high-amplitude AE events. Horsetail cracks and anti-wing cracks exhibit comparable displacement jumps in both normal and tangential directions, suggesting a mixed tensile-shear mode of crack propagation.

Keywords Stepwise cyclic loading · Flawed rocks · Energy density · Damage and fracturing process

Introduction

Rock masses play a crucial role in various engineering applications, such as hydropower, petroleum, mining, and underground structures. These rocks are often subjected to external stress disturbances resulting from earthquakes, blasting, and drilling, which can cause significant damage and dynamic failures, such as spalling, buckling, collapse, and rockburst (Cerfontaine and Collin 2017). Since the 1960s, cyclic loading has been applied to simulate the responses of rocks or slopes under repeated cyclic loads or stress disturbances caused by drilling processes and earthquakes (Burdine 1963; Haimson and Kim 1972; Hashash et al. 2001). Moreover, there is an urgent need for ongoing investigations on rock damage and fracturing under cyclic loading to enhance rock-cutting technologies (Karekal and Hood 2011) or hydraulic fracturing (Zang et al. 2021). Related research results can also be applied to evaluate the stability of rock engineering concerning variations in the water level (Sorgi and Gennaro 2011), freeze–thaw cycles (Zhang et al. 2004), and the successive emptying and filling of oil and gas storage in salt mines (Zhao et al. 2021).

The propagation of stress waves induced by earthquakes, blasting, and drilling events is complex and exhibits significant variations in characteristics. These variations are influenced by factors such as the distance from the seismicity or shock source (Zhu et al. 2007; Ramulu et al. 2009), as well as the focal mechanism and propagation direction of waves (Zhang 2016). Therefore, researchers simplified this stress disturbance as cyclic loads with different upper or lower

✉ Peng-Zhi Pan
  pzpan@whrsm.ac.cn

[1] State Key Laboratory of Geomechanics and Geotechnical Engineering, Institute of Rock and Soil Mechanics, Chinese Academy of Sciences, Wuhan, Hubei 430071, China

[2] University of Chinese Academy of Sciences, Beijing 100049, China

[3] Escuela de Ingenieria Quimica, Pontificia Universidad Católica de Valparaíso, Valparaíso, Chile

stress limits, amplitude, and frequencies in laboratory tests (Xiao et al. 2010; Han et al. 2020; Miao et al. 2021a). It has been found that low frequency and high amplitude are considered to be adverse factors to the stability of rocks, leading to a high increase rate of the stable crack propagation stage and a high proportion of the accelerated crack propagation stage (Xiao et al. 2009; Miao et al. 2021a). In addition, previous studies have identified two types of stress paths used in cyclic loading tests: constant stress amplitude and incremental amplitude applied step by step (Meng et al. 2016; Peng et al. 2019c; Yang et al. 2020b). Cyclic loading tests with a constant amplitude are commonly employed to determine the fatigue properties of rocks while increasing amplitudes are typically utilized to investigate their damage properties (Cerfontaine and Collin 2017).

Studies on the mechanical properties and damage evolution of intact rock masses under cyclic loads with a constant amplitude have been extensively reported in the literature. The degradation and damage evolution of rocks can be characterized by variations in their physical and mechanical properties, such as residual strain (Liu and He 2012; Geranmayeh Vaneghi et al. 2020), elastic or secant modulus (Momeni et al. 2015; Peng et al. 2019b), Poisson's ratio (Taheri et al. 2016; Zhu et al. 2020), P-wave velocity (Yang et al. 2020a), and permeability (Duan et al. 2020; Yang et al. 2020a). The damage and cracking of rocks are a process of energy dissipation; hence, the dissipated energy during cyclic tests has also been employed as an index for evaluating the damage of rocks (Meng et al. 2016). Besides, the damage evolution of rocks under cyclic loading tests typically exhibits three stages, namely, fatigue crack formation, stable crack propagation, and unstable crack propagation leading to sudden breakdown (Momeni et al. 2015). During constant-amplitude cyclic loading tests, the determination of the fatigue limit holds great significance. The fatigue limit is defined as the stress amplitude at which no specimen failure occurs, resulting in an infinite fatigue life (Cerfontaine and Collin 2017). However, the evolution of damage and fatigue life are highly sensitive to the mechanical properties and microstructure of rocks. As a result, there are variations in fatigue responses among rock specimens obtained from the same rock block, introducing uncertainties in determining the fatigue limit (Taheri et al. 2015). This also poses great challenges to comparing the rock damage and crack development under different stress amplitudes.

The existence of voids, joints, faults, and fractures in rock formations can lead to stress concentration, thereby increasing the likelihood of instability and failure. The failure mechanism of rocks under cyclic loads is known to be associated with the repetitive opening and closing of existing cracks, as well as the formation of new cracks due to progressive stress corrosion. This mechanism is more intricate compared to the failure observed under monotonic loading conditions (Cerfontaine and Collin 2017). In recent years, there has been growing interest in understanding the mechanical properties and damage evolution of flawed rock masses subjected to cyclic loading. Liu et al. (2017) conducted experiments to investigate the fatigue mechanical properties of intermittently flawed rock-like specimens under cyclic uniaxial compression. Their findings indicated that higher upper stress limit and amplitude, or lower loading frequency, led to increased cumulative damage and reduced fatigue life. Similarly, Zheng et al. (2020) examined the fatigue and damage characteristics of flawed mudstone under cyclic triaxial loading tests at different frequencies. Additionally, Peng et al. (2019a) focused on the influence of crack angles on the energy behavior of flawed sandstones under constant-amplitude signals. These studies underscore the limited research on the cracking behavior of flawed rock masses under cyclic loading, primarily focusing on mechanical properties. Furthermore, given the natural presence of various discontinuities in rocks, the initiation and propagation of these discontinuities play a key role in fatigue failure. Thus, comprehending the fracturing process of flawed rocks under cyclic loading conditions is critical for understanding the fatigue mechanism of rocks.

To address the aforementioned issues, we conducted uniaxial stepwise cyclic loading tests on sandstone specimens containing a single flaw. These tests aimed to investigate the evolution of damage and fracturing processes in flawed rocks. Stepwise cyclic loading offers several advantages for studying rock damage and fracturing (Cerfontaine and Collin 2017; Peng et al. 2019a). One advantage of stepwise cyclic loading is its ability to quickly determine the stress amplitude at which rock damage or fracturing occurs. By systematically increasing the stress amplitude in a stepwise manner, we can observe and analyze the point at which the rock specimen starts to exhibit damage or failure. This provides valuable insights into the critical conditions during cyclic loading (Liu et al. 2017). Moreover, stepwise cyclic loading allows us to study the impact of different stress amplitudes and the number of cycles on rock damage and fracturing using a single rock specimen. This approach eliminates the influence of rock heterogeneity when using multiple specimens. By manipulating the stress amplitude, we can examine its effects on the magnitude and progression of rock damage, thereby establishing a connection between loading conditions and subsequent rock response. Additionally, we considered flaw inclinations ranging from 0° to 90° at intervals of 15°. The damage and fracturing process of the rocks were monitored using a combination of digital image correlation (DIC) and acoustic emission (AE) techniques. The structure of the paper is as follows: the "Specimen preparation and test procedure"

section describes the preparation and testing of the specimens. In the "Results" section, we thoroughly analyze the experimental results, including stress–strain curves, energy characteristics, acoustic characteristics, and crack development. Finally, in the "Conclusions" section, we summarize the conclusions drawn from this study.

Specimen preparation and test procedure

Rock specimen preparation

Sandstone samples collected from Sichuan, China, were used for uniaxial stepwise cyclic loading tests. A polarizing microscope was used to determine the mineral particle size and composition. The sandstone was found to be predominantly composed of quartz (70%), fillers (approximately 20%), detritus (about 9%), and a minor amount of biotite (about 1%), as depicted in Fig. 1b. Table 1 lists the physical and mechanical properties of Sichuan sandstone.

Cuboid-shaped specimens were cut from an intact block, measuring 100 mm in height, 50 mm in width, and 30 mm in thickness, all in the same orientation to eliminate the effects of anisotropy (Fig. 1a). The length errors of all samples were less than 1.5 mm. The surface roughness deviation was controlled within ± 0.05 mm, and the deviation of perpendicularity between adjacent surfaces was not greater than 0.25°. A straight flaw was created in the center of specimens parallel to the specimen thickness, having a length of 20 mm and an aperture of 1.5 mm. Different flaw inclination angles α ranging from 0° to 90° at an interval of 15° were considered, and three rock specimens were prepared for each geometry. The rock specimens were named with flaw inclination angle and number, for instance, "S30-1" corresponds to the first prepared sandstone specimen with a flaw inclined at 30°. Before testing, the integrity of the specimens was verified, and a random speckle pattern was applied to the specimen surfaces by spraying black and white paints for DIC analysis. As shown in Fig. 1a, the speckle pattern

Fig. 1 **a** Dimensions of flawed sandstone specimens, location of AE sensors, and speckle pattern on rock specimen, and **b** microscopic observation of mineral particles in sandstone specimens (quartz—Qtz, biotite—Bt)
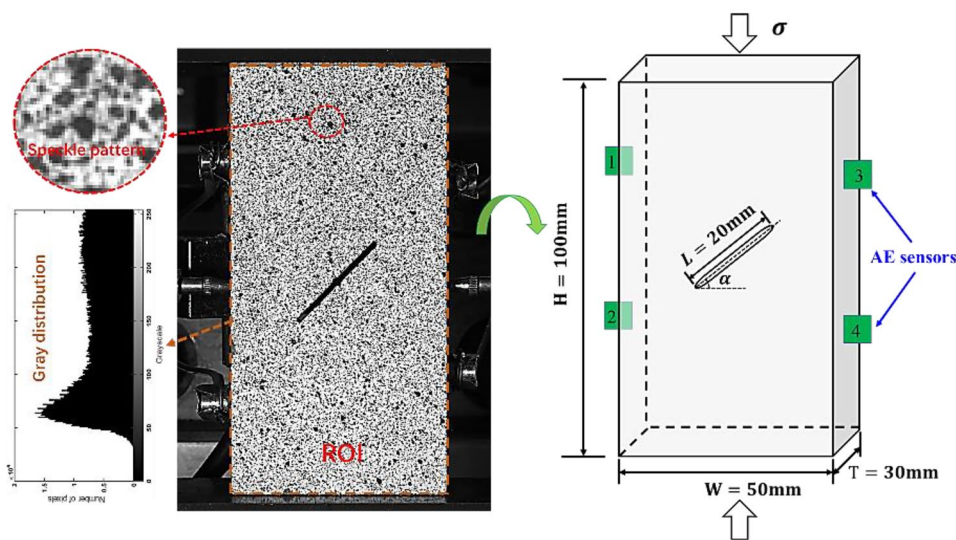
(a)
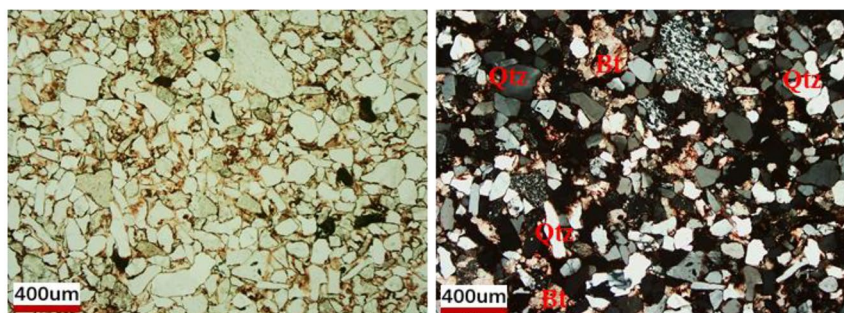
(b)

Table 1 Physical and mechanical properties of Sichuan sandstone

Rock type	Mineral composition	Grain size (mm)	Density (g/cm3)	UCS (MPa)	Young's modulus (GPa)	Poisson's ratio
Sandstone	70% quartz, 20% filler, 9% detritus, and 1% biotite	0.06 ~ 0.30	2.13 ~ 2.28	70 ~ 75	12.5 ~ 13.6	0.19 ~ 0.22

employed in our study demonstrated a grayscale distribution ranging from 30 to 255. This range provides adequate contrast between the speckles and the background, facilitating accurate tracking and measurement of deformation. Additionally, note that the distribution of gray values was uniformly spread across the pattern, avoiding any significant concentration of dark or light areas. To minimize the friction with the loading plates, the upper and lower ends of the specimen were lubricated before each test.

Experimental equipment

Uniaxial stepwise cyclic loading tests were conducted using an electro-hydraulic servo-controlled rock mechanics testing system (MTS 815.03) at the Institute of Rock and Soil Mechanics, Chinese Academy of Sciences, Wuhan. The system is capable of performing static and dynamic compression testing on rock specimens, with a maximum vertical load of 4600 kN and a maximum vertical piston stroke of 100 mm. Axial load was measured with a load cell and axial displacement was measured with a linear variable differential transformer. The load and displacement data were collected using a data acquisition system with a sampling interval of 0.02 s.

To monitor rock damage and fracturing, DIC and AE techniques were used together. The device used for recording digital images comprised a CCD camera with a resolution of 3376×2704 pixels, two white light sources, and a computer with image acquisition software. The CCD camera sensor was fixed perpendicular to the specimen surface to record high-resolution digital images. The image acquisition software recorded a sequence of images at a rate of 9 frames per second. The AE monitoring system included four AE sensors (PAC, Nano 30), four preamplifiers, and a 16-channel monitoring board (PCI-2, PAC). The AE sensors were attached directly to the specimen surfaces with grease to ensure good acoustic coupling. Adhesive tapes were used to ensure good contact between the rocks and sensors. The threshold and pre-amplifier gain were set to 40 dB, and the AE signals were recorded at a sampling rate of 2 MHz.

Loading path

The study applied sinusoidal waveforms to the specimens in uniaxial stepwise cyclic compression tests. The upper-stress limit was incrementally increased by 5 MPa at each stress level, while the lower stress limit was set to 0.5 MPa to ensure proper contact between the loading device and the rock specimen. To study the damage evolution and cracking behavior under repeated loads, five cycles were repeated at each stress level. The frequency of the sinusoidal waveform varied in each stress level to maintain an average loading and unloading rate of 1 MPa·s^{-1} in each cycle, thus eliminating the effects of loading rate during stepwise cyclic tests. As a result, the loading time for each stress level depended on the applied maximum axial stress. For instance, the frequency was set to 0.1 Hz for the first stress level with a maximum stress of 5 MPa, and then decreased to 0.05 Hz for the second stress level with a maximum stress of 10 MPa, and so on. The stepwise cyclic loading was executed automatically according to a prewritten program until the specimen failed (Fig. 2).

Results

Stress–strain curves

Figure 3 displays stress–strain curves for flawed rock specimens with a single flaw under uniaxial stepwise cyclic loading. The curves for flawed specimens with various flaw inclination angles show a similar evolution pattern. Unlike elastic materials, rock materials with various defects exhibit a hysteresis loop in the stress–strain curves. The loading and unloading process within a cycle may induce damage and fractures within rocks, with the unloading paths not coinciding with the reloading paths. The hysteresis loop is pronounced in the first cycle due to the compaction effect of voids, defects, pre-existing flaws, or crack extension induced by sudden increases in the maximum stress limit. The irreversible deformation accumulates as the number of cycles or stress levels increases, and the generation of several macro cracks can cause great irreversible deformation and hysteresis loop areas. Moreover, a sudden loose pattern of the stress–strain curves is observed in the last few cycles.

Fig. 2 Illustration of the stepwise cyclic loading path applied to the flawed rock specimens
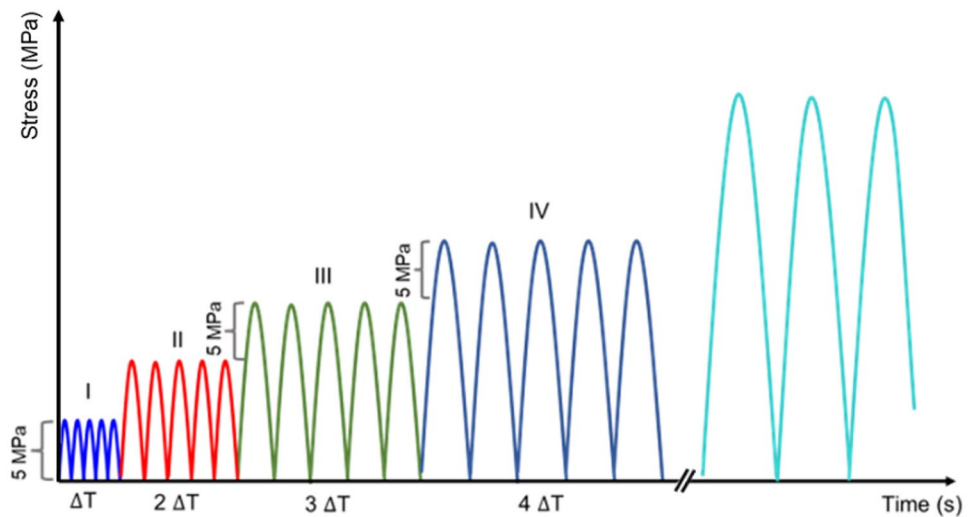
Figure 4 shows that the failure stress of flawed rock specimens displays an increasing trend with the flaw inclination angle. The average failure stress for flawed specimens with inclination angles of 0°, 15°, 30°, 45°, 60°, 75°, and 90° is 35.65 MPa, 36.64 MPa, 43.22 MPa, 46.61 MPa, 51.01 MPa, 58.69 MPa, and 67.15 MPa, respectively. This trend is similar to that observed in flawed specimens under monotonic loading (Miao et al. 2018). This phenomenon is related to the way that the pre-existing flaw affects the distribution of stress within the rock specimen. The correlation between failure stress and flaw inclination angle can significantly contribute to the advancement of more precise failure criteria specifically designed for flawed rock masses subjected to cyclic loading.

Energy evolution

Elastic strain energy refers to the amount of energy stored in a rock material due to the application of external stresses, which is released when the stresses are removed. The amount of elastic strain energy stored in a rock depends on its elastic properties, which are determined by its composition, structure, and physical properties. The degradation of rock materials is often associated with energy dissipation (Xie et al. 2004; Liu et al. 2016; Li et al. 2020). Energy dissipation can occur due to various factors such as frictional forces between fracture surfaces, plastic deformation of the rock, and the formation and propagation of cracks within the rock. The dissipated strain energy can be considered to be a damage variable that can be used to evaluate the degradation behavior of rock materials (Liu et al. 2017). Assuming that there is no heat exchange between the rock specimens and the surrounding environment, the total input energy U can be expressed as the sum of the elastic strain

energy U^e that can be recovered during deformation and the dissipated strain energy U^d that is utilized for generating internal damage and irreversible deformation of rocks, which can be described as:

$$U = U^e + U^d \qquad (1)$$

According to Xie et al. (2005), the strain energy of rocks can be further characterized by the strain energy density:

$$\int u dV = \int u_e dV + \int u_d dV \qquad (2)$$

where u, u_e, and u_d represent the total energy density, the elastic energy density, and the dissipated energy density of the rock, respectively; V is the volume of rocks.

The strain energy density can be calculated by integrating the stress–strain curve. As shown in Fig. 5, the total energy density u, the elastic energy density u_e, and the dissipated energy density u_d of the rock in a cycle can be computed as follows (Meng et al. 2016; Peng et al. 2019a):

$$u = \int_{\varepsilon_1}^{\varepsilon_{max}} \sigma d\varepsilon = \sum_{i=1}^{n} \frac{1}{2}\left(\sigma_i + \sigma_{i+1}\right)\left(\varepsilon_{i+1} - \varepsilon_i\right) \qquad (3)$$

$$u_e = \int_{\varepsilon_2}^{\varepsilon_{max}} \sigma d\varepsilon = \sum_{i=1}^{n} \frac{1}{2}\left(\sigma_i' + \sigma_{i+1}'\right)\left(\varepsilon_{i+1}' - \varepsilon_i'\right) \qquad (4)$$

$$u_d = u - u_e \qquad (5)$$

where ε_1 and ε_2 denote the axial strains at the minimum stress of the loading and unloading stages, respectively, while ε_{max} represents the strain at the maximum stress for each cycle. σ_i, σ_{i+1}, ε_i, and ε_{i+1} are the stress and strain at an integral step in the loading stage, whereas σ_i', σ_{i+1}', ε_i', and ε_{i+1}' are the stress and strain for an integral
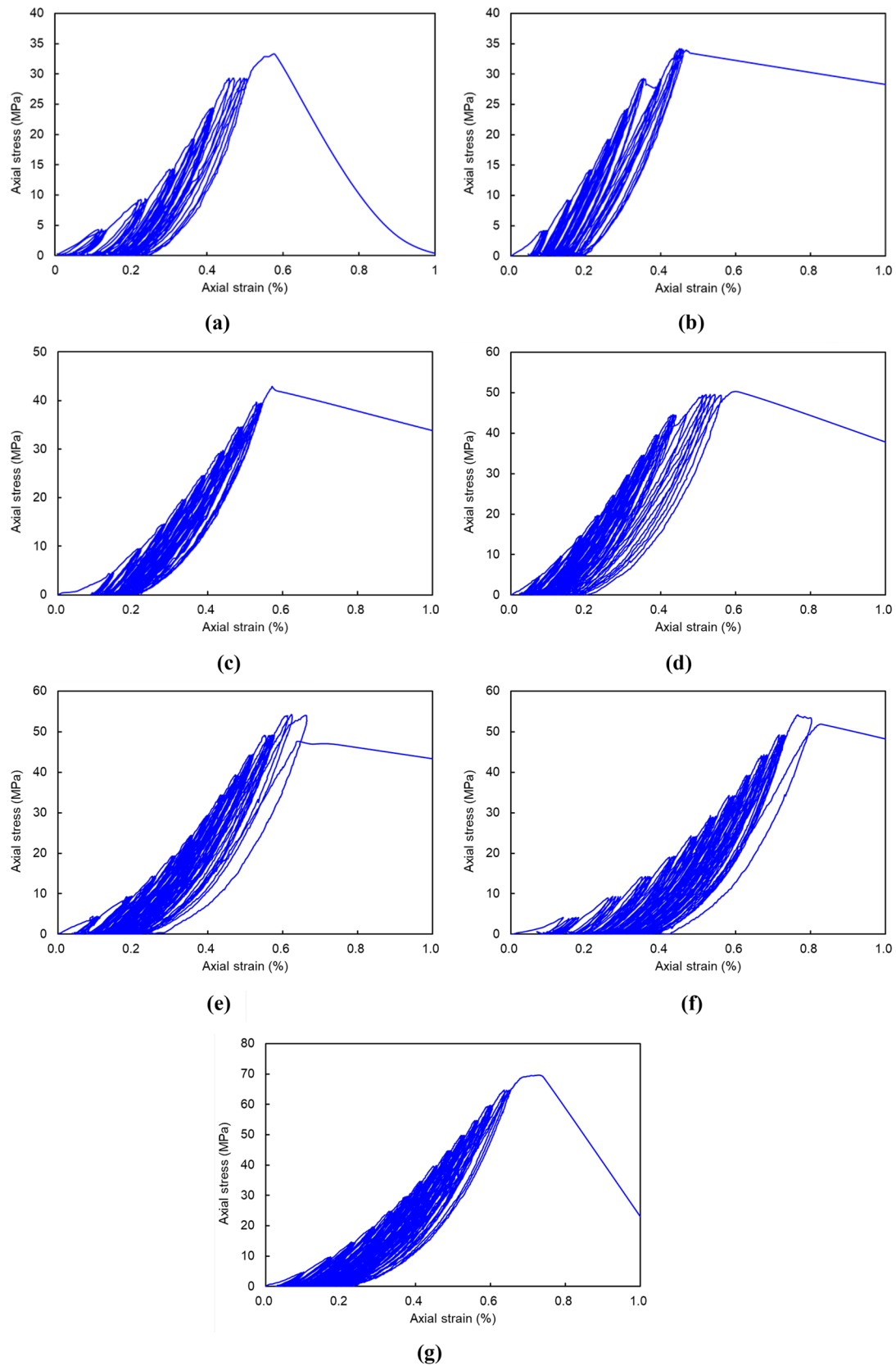
Fig. 3 Stress–strain curves for sandstone specimens containing a single flaw at various inclination angles: **a** S0-1, $\alpha=0°$, **b** S15-1, $\alpha=15°$, **c** S30-1, $\alpha=30°$, **d** S45-1, $\alpha=45°$, **e** S60-1, $\alpha=60°$, **f** S75-1, $\alpha=75°$, and **g** S90-1, $\alpha=90°$
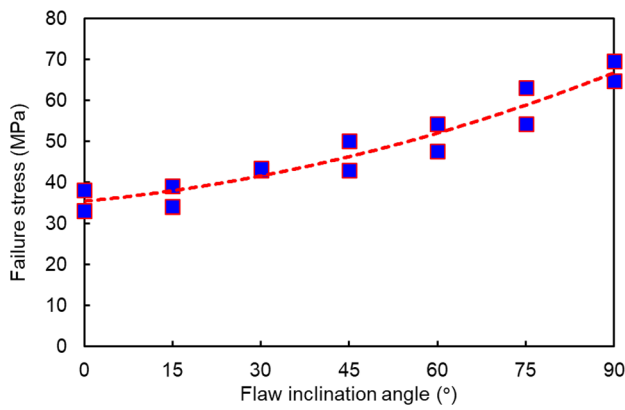
Fig. 4 Variation in failure stress with the increasing flaw inclination angle

step in the unloading stage. The total number of integral steps is denoted by n.

Figure 6 depicts the strain energy density for flawed specimens with varying flaw inclination angles during stepwise cyclic loading. When the flawed rock specimen is subjected to greater stress levels, more elastic deformation will occur, resulting in more energy being stored within the rock specimen. On the other hand, the bonds between grains within the rock are broken during plastic deformation, leading to the change of the rock's internal structure. As the stress level increases, more and more bonds within rocks are broken, leading to greater plastic deformation and more energy dissipation. Therefore, the results indicate that both the elastic energy density (u_e) and dissipated energy density (u_d) in each cycle significantly increase as the applied stress level increases, as shown in Fig. 6.

When rocks are subjected to repeated cyclic loading, they exhibit strong memory properties, meaning that the mechanical behavior of the rock is influenced by its past loading history. Figure 6 illustrates that the total energy density and dissipated energy density typically decrease with an increase in the number of loading cycles for a given loading
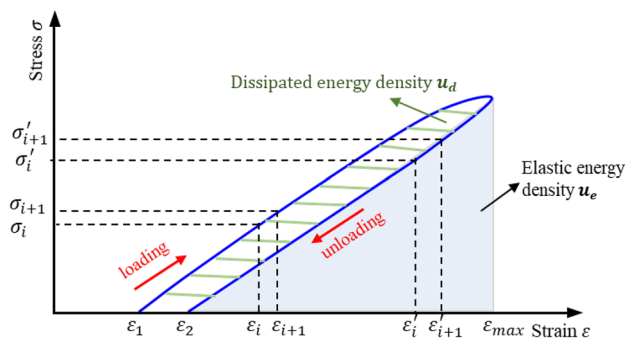

Fig. 5 Schematic diagram for strain energy density calculation using the stress–strain curve

level. This phenomenon is often referred to as cyclic fatigue or cyclic softening. The repeated cycles cause the accumulation of microscopic damage and irreversible deformation, leading to a reduction in the rock's strength and stiffness. As a result, the amount of energy that can be stored in the rock decreases with the increasing cycle, leading to a decrease in the total energy density. Additionally, the dissipated energy density also decreases with an increase in the number of cycles. This is because as the rock becomes more damaged and deformed, the energy required to cause further deformation decreases. As a result, less energy is dissipated during each loading cycle, leading to a decrease in the dissipated energy density. Compared to the total energy density and dissipated energy density, the elastic energy density changes slightly with the number of cycles.

As the applied stress level increases, the difference between the elastic energy density and dissipated energy density becomes more significant, as depicted in Fig. 6. This is because, the material store more elastic energy at higher stress levels before it starts to generate noticeable irreversibly deform or crack, resulting in a larger difference between the two types of energy densities. Despite the increasing difference between the elastic and dissipated energy densities as the stress level increases, the dissipated strain energy in each cycle still experiences an increase for all rock specimens. This indicates that as the stress level increases, the material experiences more irreversible deformation and cracking.

To investigate the energy dissipation behavior of flawed rock specimens under different stress levels, a dissipation factor is defined as the ratio of the dissipated energy density to total energy density. The variations of the dissipation factor with upper stress limit for flawed specimens under different flaw inclination angles (0°, 30°, and 75°) are presented in Fig. 7a–c. It is observed that the dissipation factor initially decreased with increasing upper stress limit and then stabilized at a constant value. At lower stress levels, there is a significant difference in the dissipation factor among the five cycles, but as the stress levels increased, this difference decreases, indicating a more consistent energy dissipation behavior of the flawed rock specimens in different cycles. The dissipation factor at the first cycle is generally higher than the other four cycles, implying a memory effect of the rocks. Additionally, Fig. 7d illustrates the variation of the dissipation factor with the flaw inclination angle. The average and median dissipation factor decrease initially and then increase as the flaw inclination angle increased from 0° to 90°, and flaws perpendicular to the compression direction of the rock specimen lead to a higher dissipation factor. Figures 6 and 7 demonstrate that a greater crack angle in rocks enhances the energy storage capacity but slightly weakens the energy dissipation capacity, leading to increased energy demand for rock failure and higher peak strength during
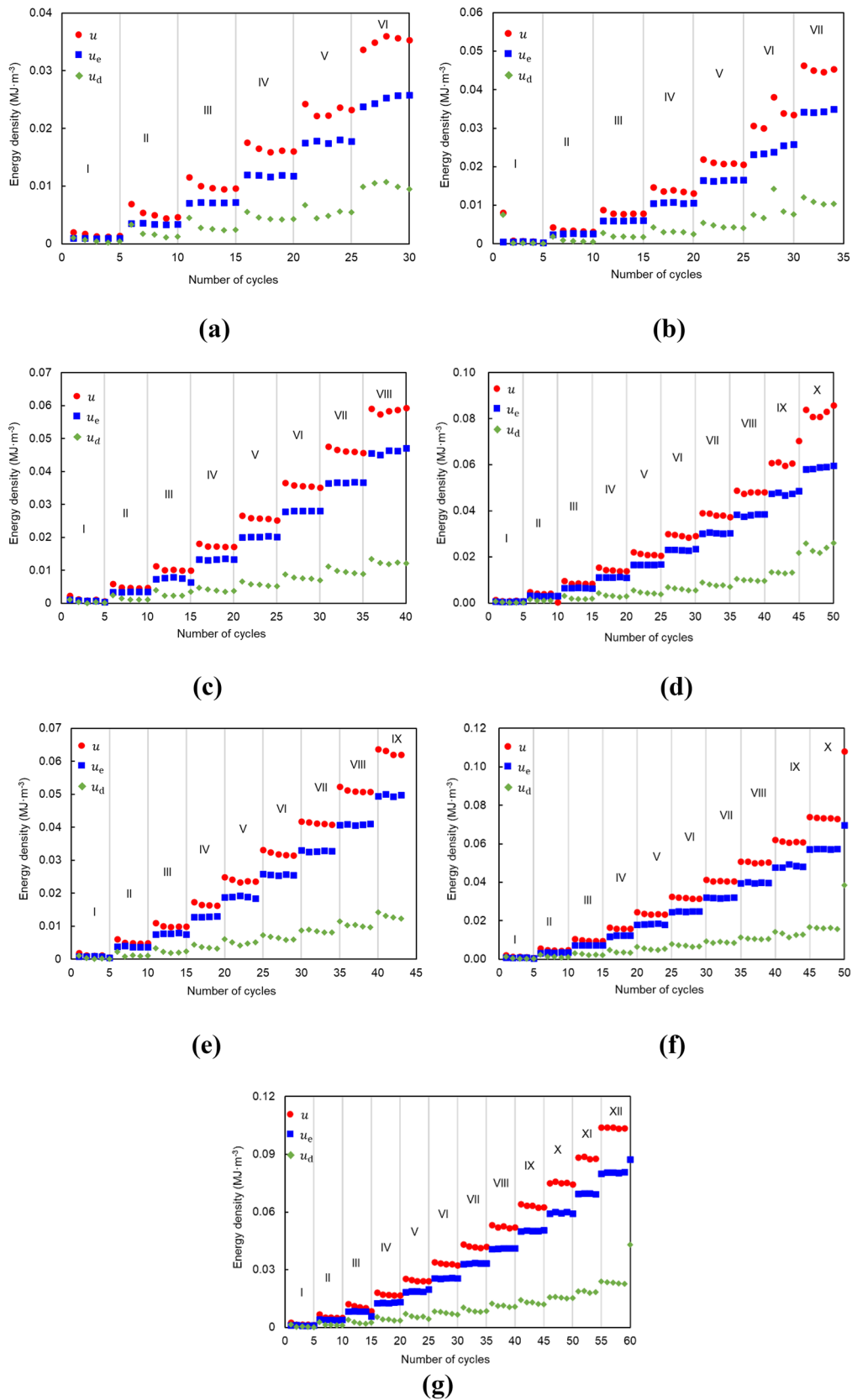
Fig. 6 Strain energy density in each cycle for flawed specimens with different flaw inclination angles during stepwise cyclic loading: **a** S0-1, $\alpha = 0°$ **b** S15-1, $\alpha = 15°$ **c** S30-1, $\alpha = 30°$ **d** S45-1, $\alpha = 45°$ **e** S60-1, $\alpha = 60°$ **f** S75-1, $\alpha = 75°$ **g** S90-1, $\alpha = 90°$
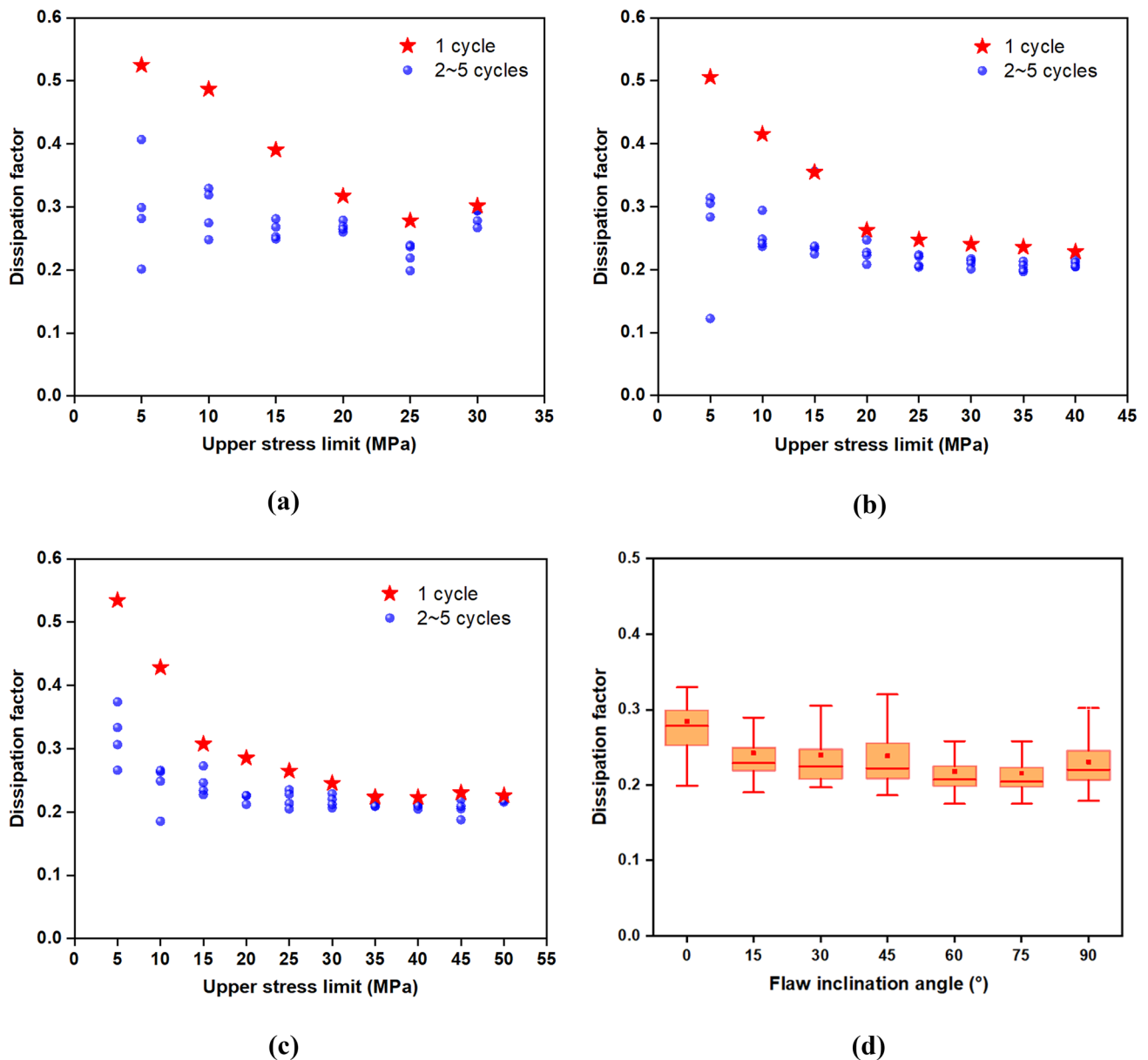
Fig. 7 Variations of dissipation factor with upper stress limit and flaw inclination angle: **a** –**c** changes in dissipation factor with upper stress limit for flawed specimens inclined at 0°, 30°, and 75°, respectively, and **d** variation of dissipation factor with flaw inclination angle

failure. This phenomenon clarifies the correlation between crack angle and the energy-based bearing capacity of rocks, providing valuable insights for the instability assessment of flawed rock engineering.

Figure 8 shows the cumulative dissipated energy density during the stepwise cyclic loading process, which exhibits a quadratic increase with the increasing number of cycles. The growth rate of the accumulative dissipated energy density (CDED) increases as the stepwise cyclic loading proceeds, indicating that damage within the rocks accumulates at an

increasing rate. The cumulative dissipated energy density for rock specimens with a flaw inclined at $\alpha = 0°$, 15°, 30° is 0.127 MJ·m^{-3}, 0.149 MJ·m^{-3}, 0.210 MJ·m^{-3}, respectively. For rock specimens containing a flaw inclined at $\alpha = 45°$, 60°, 75°, 90°, the cumulative dissipated energy density during stepwise cyclic loading is 0.368 MJ·m^{-3}, 0.408 MJ·m^{-3}, 0.381 MJ·m^{-3}, 0.587 MJ·m^{-3}, respectively. These results suggest that rock specimens with a greater inclination angle dissipate more strain energy before rock rupture compared to those with a smaller inclination angle.

Fig. 8 CDED for flawed sandstone specimens during the stepwise cyclic loading process: **a** $\alpha=0°$, 15°, and 30°, **b** $\alpha=45°$ and 60°, and **c** $\alpha=75°$ and 90°

(a)

(b)

(c)
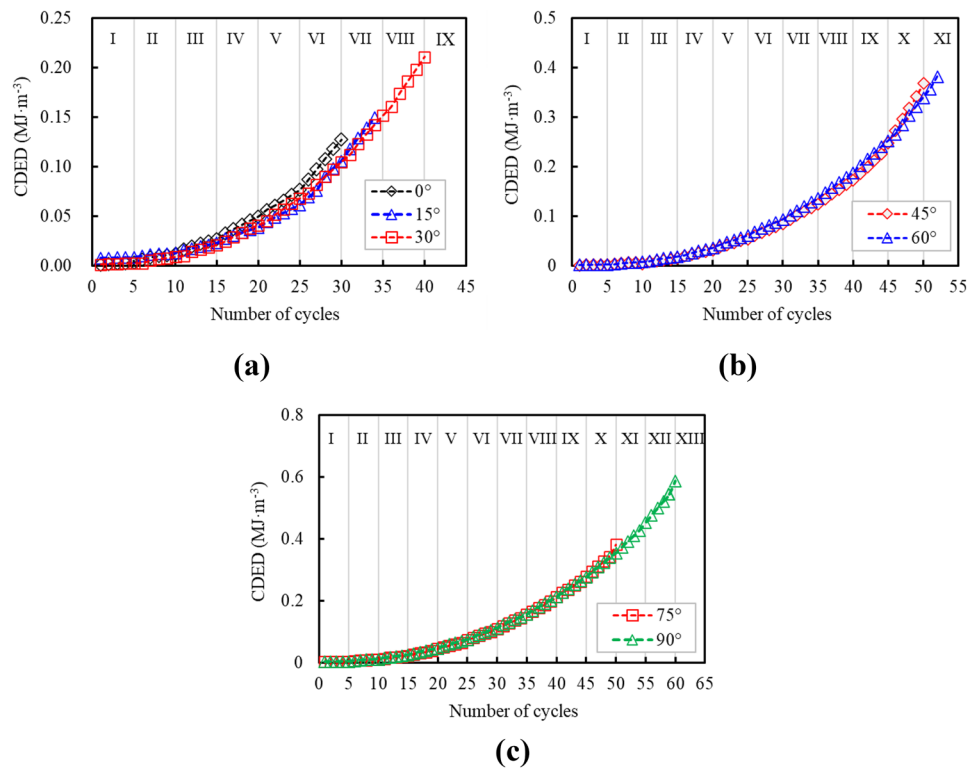
Failure characteristics

AE techniques provide valuable information on the internal damage of rock materials and can help researchers understand the failure mechanisms. The evolution of AE count rate and cumulative AE counts for flawed rock specimens under stepwise cyclic loading is shown in Fig. 9. The AE evolution for flawed specimens during the stepwise cyclic loading process can generally be divided into two stages: the stable crack propagation stage (stage I) and the accelerated propagation stage (stage II). For example, in Fig. 9a, the AE responses for the flawed specimen S0-1 containing a flaw inclined at 0° show that the AE activity in the accelerated crack propagation stage is much more active than in the stable crack propagation stage. At stage I, a relatively high peak of the AE count rate is observed in the first cycle of a specific stress level, while the AE count rate decreases greatly in the remaining four cycles, indicating that the AE signals within the stable crack propagation stage conform to the Kaiser effect. The cumulative AE counts present a small-magnitude rise at the first cycle of these stress levels, followed by an approximately linear increase in the remaining four cycles. In the accelerated crack propagation stage, the AE count rate exhibits several high peaks, and the cumulative AE counts present a stepwise growth until the specimen fails. Besides, the peak AE count rate decreases in the first some cycles in stage II, while it dramatically increases in the final few cycles,

showing both the Kaiser and Felicity effect. Similar AE response patterns can be observed in other flawed specimens, as shown in Fig. 9b–g.

Differences in AE responses are noticed between specimens with small and large flaw inclination angles (Fig. 9a–g). The cumulative AE counts in the stable propagation stage can be viewed as a linear increase, with specimens containing a flaw inclined at 0°, 15°, and 30° having a much steeper slope than those with a flaw inclined at 45°, 60°, 75°, and 90°. In specimens with greater flaw inclination angles, the AE events are mostly clustered in the last few cycles, indicating that the rapid crack propagation and instability take place in a short period. The differences in AE distribution are closely related to the initiation and propagation of newly formed cracks from flaw tips, which will be explained later. Overall, AE monitoring is an effective technique for measuring rock damage in flawed sandstone specimens under stepwise cyclic loading.

During stepwise cyclic compression, different types of cracks may initiate from the pre-existing flaw, such as wing cracks, horsetail cracks, coplanar cracks, and anti-wing cracks, which are named according to their shapes (Wang et al. 2017; Pan et al. 2019). To characterize the cracking behaviors during the loading process, the AE amplitude distribution and maximum principal strain contours measured by the DIC technique are presented. Figure 10b shows the cracking behaviors of specimen S15-1, which contains a flaw inclined at $\alpha = 15°$. The focus is on the nucleation,
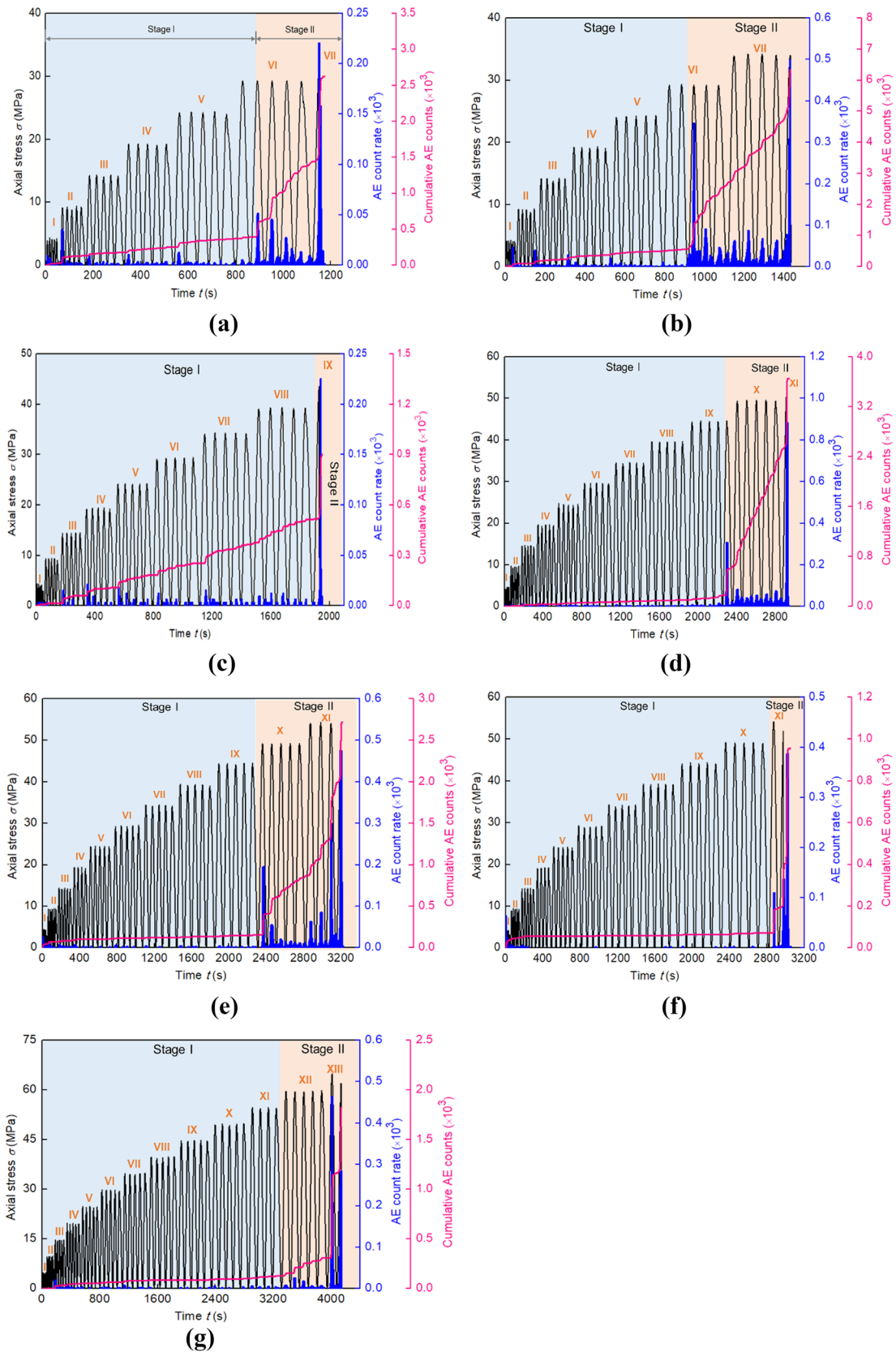
Fig. 9 AE count rate and cumulative AE counts for flawed sandstone specimens with varied flaw inclination angles **a** S0-1, $\alpha=0°$, **b** S15-1, $\alpha=15°$, **c** S30-1, $\alpha=30°$, **d** S45-1, $\alpha=45°$, **e** S60-1, $\alpha=60°$, **f** S75-1, $\alpha=75°$, and **g** S90-1, $\alpha=90°$

initiation, and propagation of new cracks under stepwise cyclic loads, and some key time instants are selected and marked in Fig. 10a, named by the stress level and the number of cycles within the stress level. For example, "II-1" denotes the specimen is at the wave peak of the 1st cycle in stress level II.

As shown in Fig. 10b, for specimen S15-1, two strain localization bands appear at the 5th cycle of stress level I (i.e., point A5), resulting from tensile stress concentration at the center of the flaw periphery. The appearance of the strain localization bands means the formation of the fracture process zone (FPZ), which contains various tensile microcracks. As the stress level increases, two high-strain bands are observed at point B5, indicating the formation of tensile wing cracks. The strain contours at points C1 and C5 show that the wing crack continuously propagates under repeated cycles. This observation is also seen at points D1, D5, and E1, E5, where the wing cracks gradually extend under repeated cyclic loads in a specific stress level. When the specimen is loaded to the peak of the 5th cycle of stress level III, four strain localization bands can be vaguely distinguished at the two flaw tips, which exhibit a fan shape and cover a large area. The fan-shaped zones result from the compression of the voids and defects and are evidence of the existence of high compressive stress. As the stress level increases, the strain within the fan-shaped zone increases, and the size of the four fan-shaped bands also expands. In stress level VI, two high-strain bands appear within two lower fan-shaped zones at the peak of the 1st cycle and abruptly develop into two anti-wing cracks at the 3rd cycle, accompanied by abundant high-amplitude AE events. The formation of two anti-wing cracks stops the propagation of two wing cracks at the flaw center and simultaneously closes one of the wing cracks. The further increase in the stress level does not significantly extend the length of the initiated anti-wing cracks. In the last few cycles, a horsetail crack initiates from the lower flaw tip and extends a short distance under cyclic loads. At the same time, some small cracks located at the lower right corner of the specimens tend to coalesce with one of the anti-wing cracks, leading to the deterioration and instability of the rocks. The detailed fracturing process observed during stepwise cyclic loading provides valuable insights for calibrating newly developed simulation approaches designed for cyclic loading in the future.

The cracking behavior during stepwise cyclic loading can also be revealed by the AE amplitude distribution. A large amount of energetic AE events takes place once the anti-wing cracks initiate and propagate, while fewer AE events are observed during the initiation and propagation of wing cracks, as shown in Fig. 10a. Most events in a stress level are clustered in the first cycle due to the increase in the stress limit, while some scattered events appear in the last four cycles for a specific stress

level, indicating that the crack extension takes place under repeated cycles.

The fracture behavior of initiated cracks in specimen S15-1 can be further analyzed using a novel DIC-based method proposed by Miao et al. (2021b). The crack paths and displacement jump over the cracks are shown in Fig. 11a at significant time instants when new cracks initiate from the flaw tips, such as C1, E1, F3, and G5. The identified crack paths in Fig. 11a are consistent with the high strain bands in strain contours shown in Fig. 10, which validates the effectiveness of the method. Displacement jumps across the initiated cracks are also measured for fracture mechanism identification.

According to classical linear elastic fracture mechanics, a crack propagates in three basic modes under plane stress loading: mode I, mode II, and mixed mode I/II (Anderson 2017). Figure 11b and c illustrates the normal and tangential displacement jumps over the initiated cracks. At points C1 and E1, significant normal displacement jumps are observed across the two wing cracks, while the tangential displacement jumps are negligible. The significant normal displacement jumps and the absence of the tangential displacement jumps indicate that the two wing cracks are tensile cracks, which is consistent with previous findings (Wong and Einstein 2009). The theoretical analysis by Lajtai (1971) also reveals that cracks initiated from the flaw center are caused by the concentration of tensile stress. At point F3, two anti-wing cracks (i.e., cracks 2# and 3#) appear, and large displacement jumps in both the normal and tangential directions are observed. This indicates that the two anti-wing cracks are mixed tensile-shear cracks. The significant tangential displacement jumps also suggest that local shear stress plays a significant role in the initiation of anti-wing cracks. In addition, four fan-shaped zones of significant size provide further evidence of the existence of high compressive stress around the flaw tips (Fig. 10b, E5). Therefore, the initiation and propagation of the two mixed tensile-shear anti-wing cracks are caused by high compressive-shear stress. Similarly, the horsetail crack (i.e., crack 4#) initiated from the lower flaw tip at point G5 is also identified as a mixed tensile-shear crack due to comparable displacement jumps in both the normal and tangential directions. It should be noted that the crack types appearing in flawed rock specimens under stepwise cyclic loads are the same as those under monotonic loading (Miao et al. 2021b).

Figure 12 illustrates the cracking behavior of specimen S45-1 under stepwise cyclic loading. The specimen remains elastic in the first two stress levels, and the formation of the FPZ is observed at the flaw tips in stress level III (Fig. 12b, A1, A5). As the stress level and the number of cycles increase, the FPZs develop into wing cracks, but unlike specimen S15-1, the wing cracks in S45-1 stop propagating after extending a shorter distance. At the first cycle of stress

Fig. 10 Cracking behaviors at significant time instants for flawed specimen S15-1: **a** stress-time curves with typical moments marked during the stepwise loading process, and **b** the maximum principal strain contours obtained from DIC technique at significant time instants
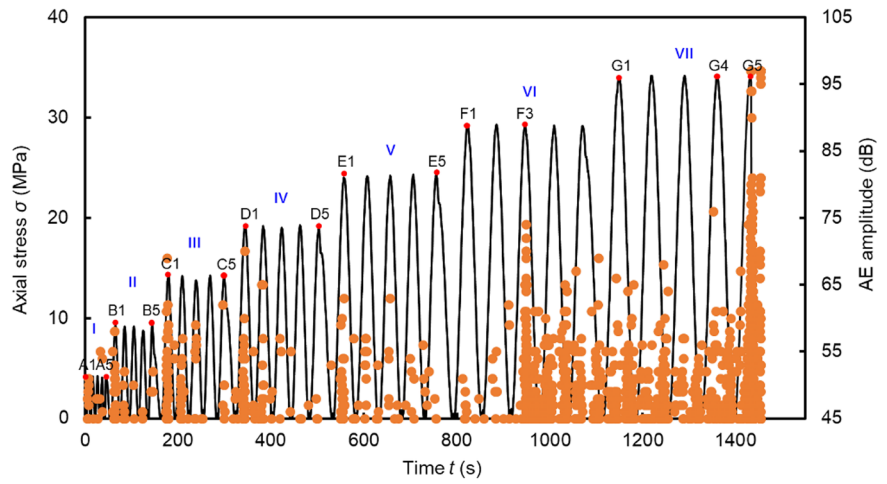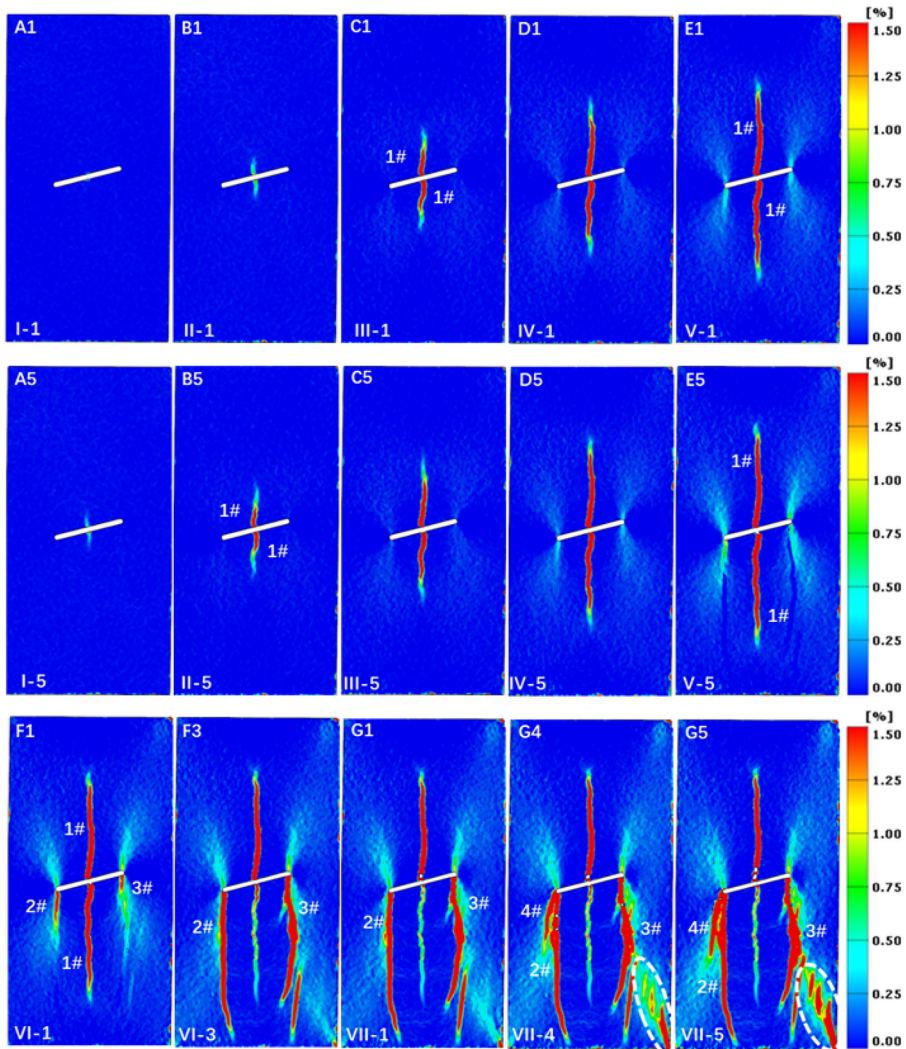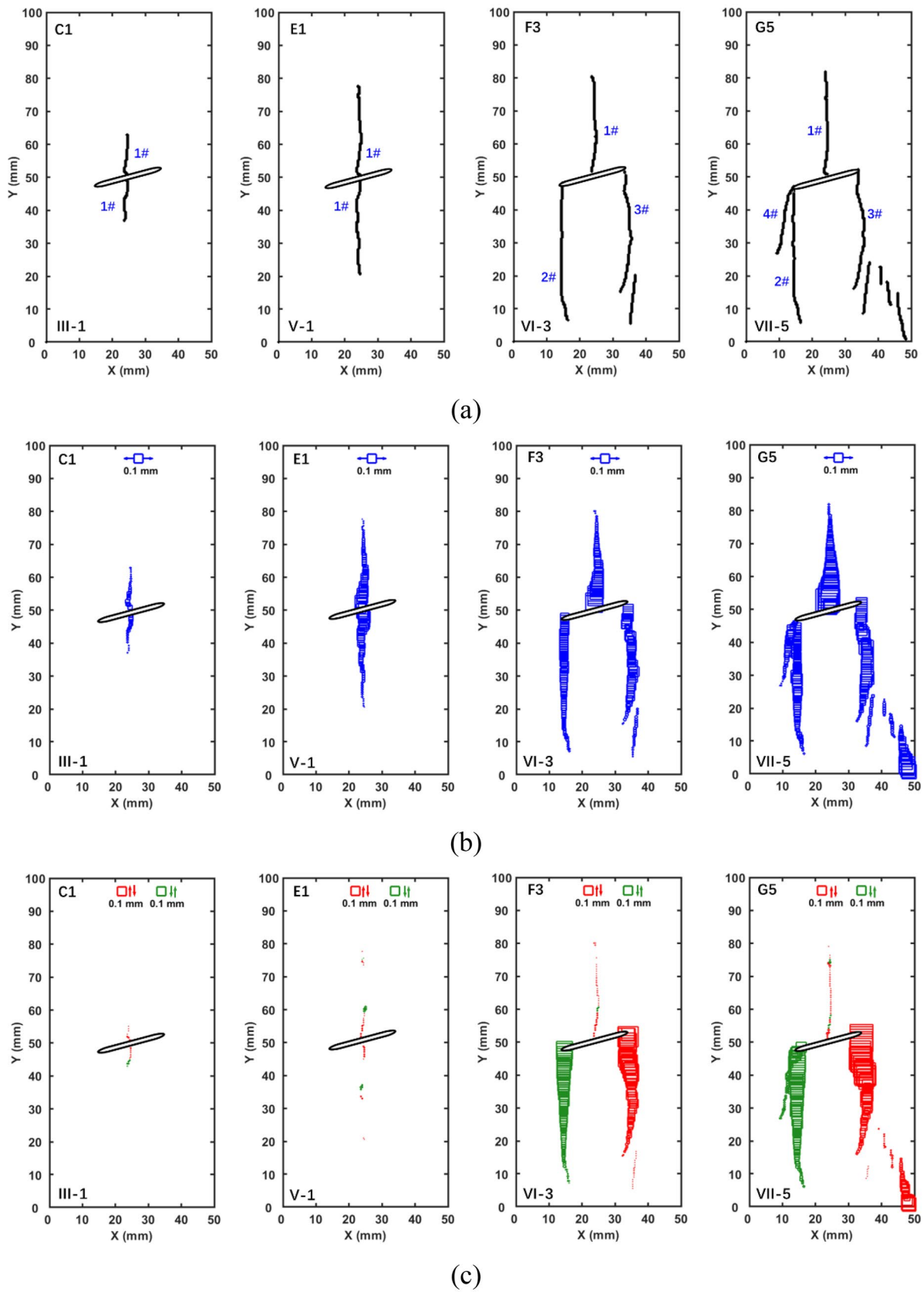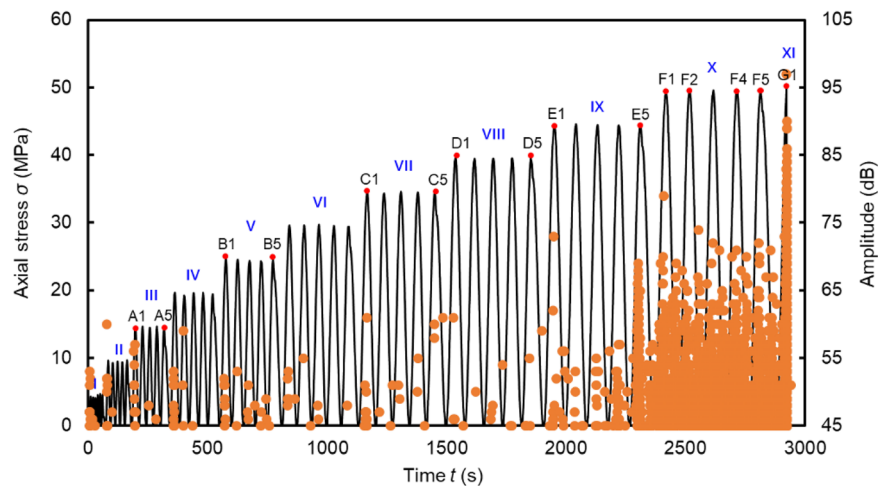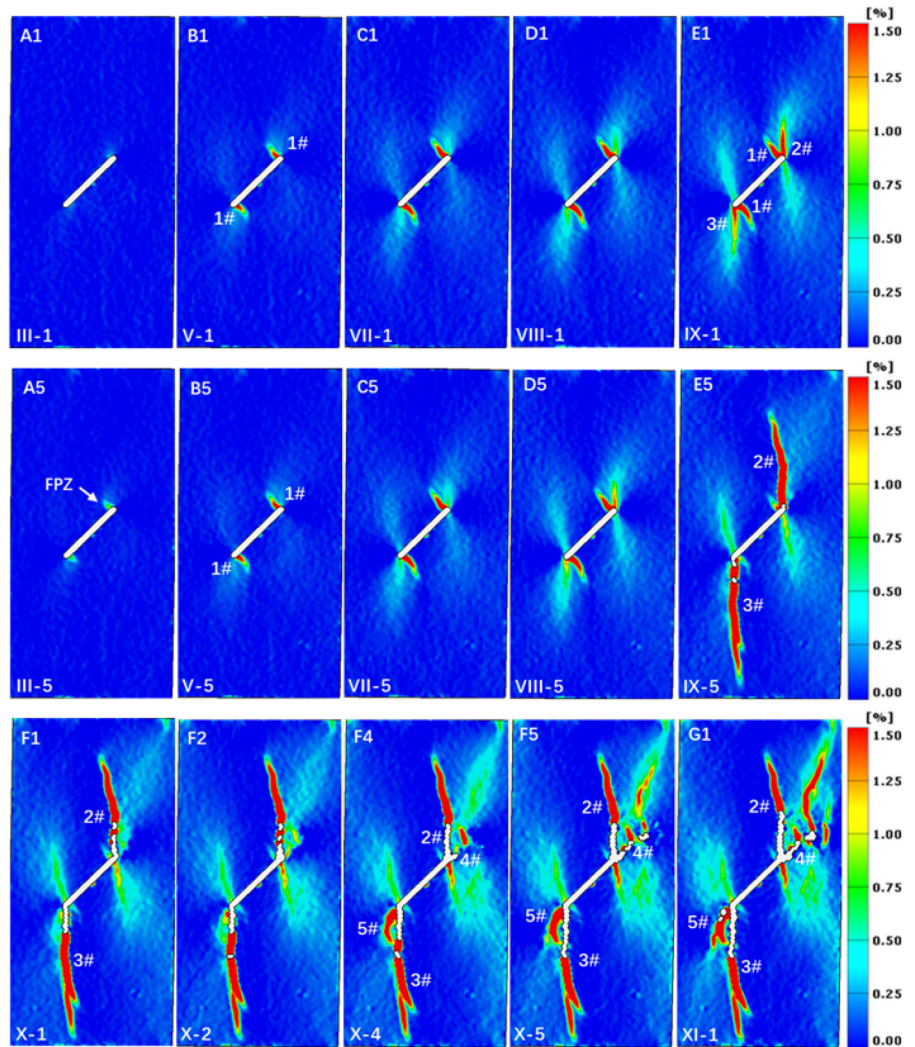
Fig. 11 Crack paths and displacement jumps over initiated cracks in flawed specimen S15-1 at significant time instants: **a** identified crack paths, **b** normal displacement jumps across cracks, and **c** tangential displacement jumps across cracks

Fig. 12 Cracking behaviors at significant time instants for flawed specimen S45-1: **a** stress-time curves with typical moments marked during the stepwise loading process, and **b** the maximum principal strain contours obtained from DIC technique at significant time instants
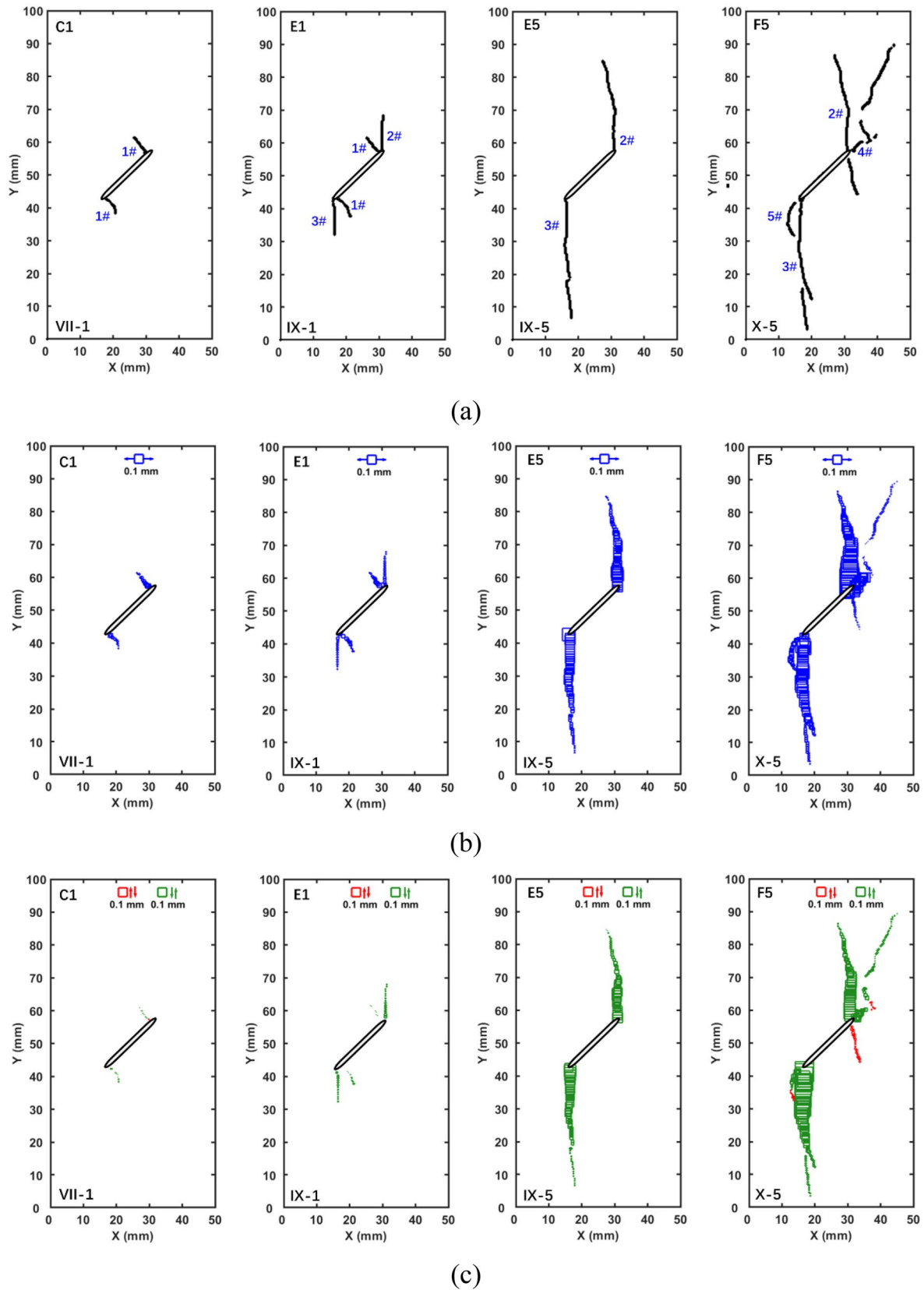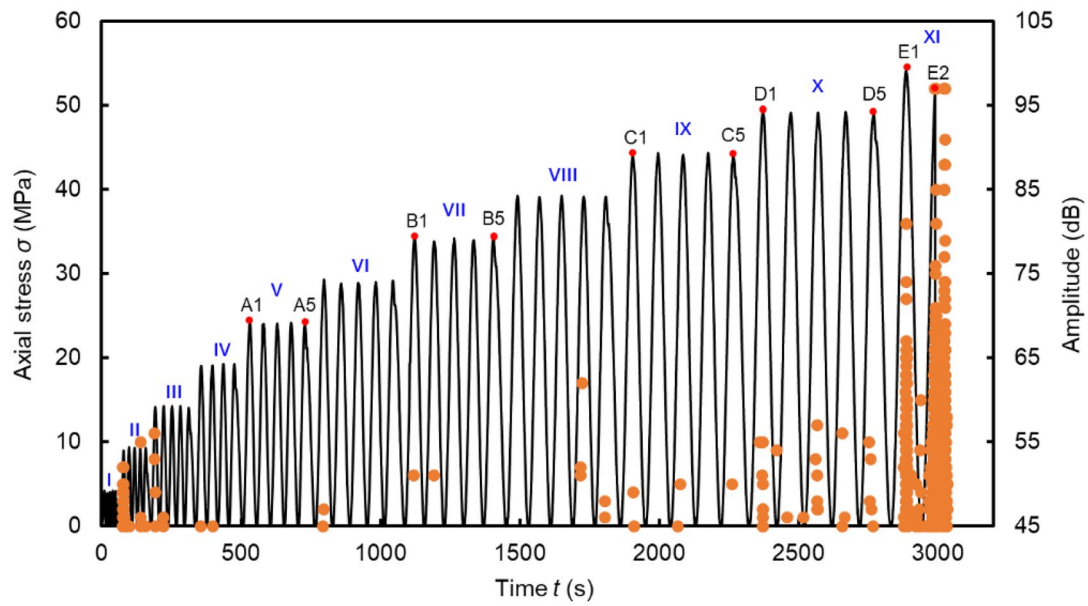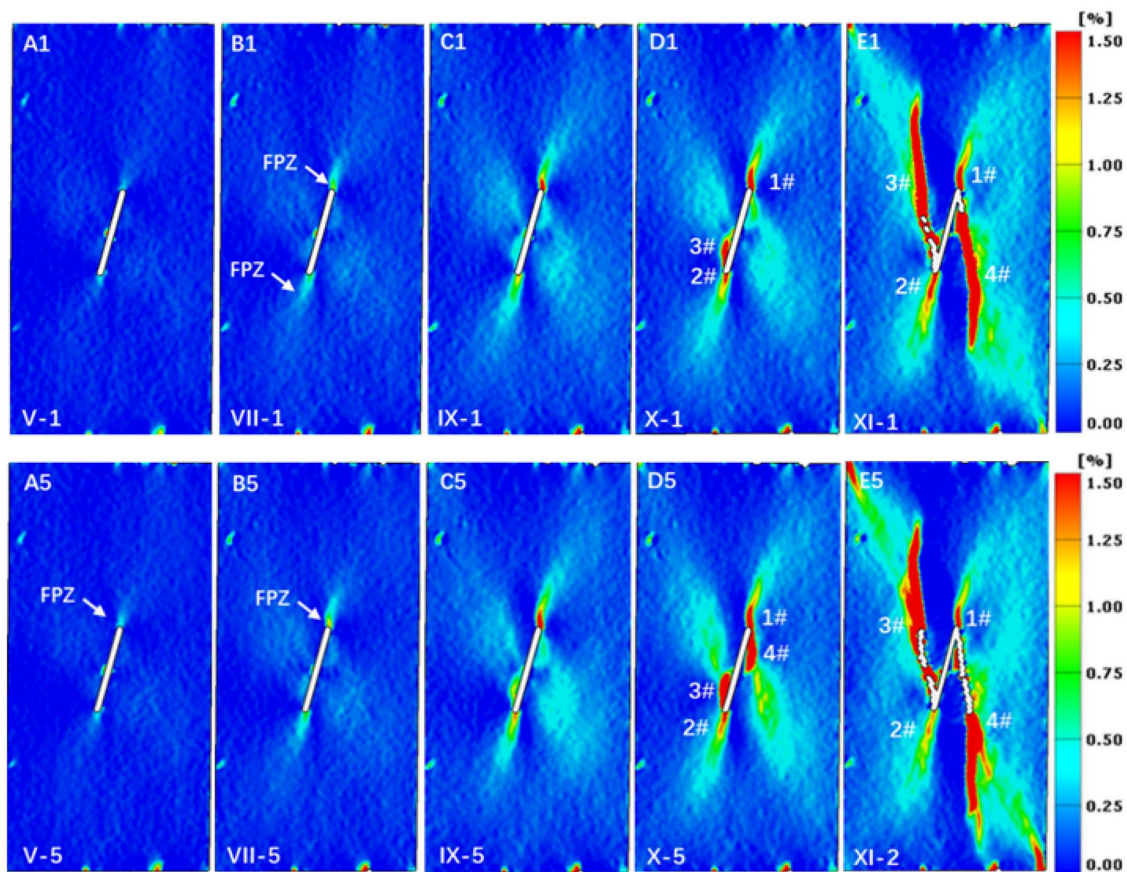

(a)

(b)

Fig. 13 Crack paths and displacement jumps over initiated cracks in flawed specimen S45-1 at significant time instants: **a** identified crack paths, **b** normal displacement jumps across cracks, and **c** tangential displacement jumps across cracks

(a)

(b)

Fig. 14 Cracking behaviors at significant time instants for flawed specimen S75-1: **a** stress-time curves with typical moments marked during the stepwise loading process, and **b** the maximum principal strain contours obtained from DIC technique at significant time instants
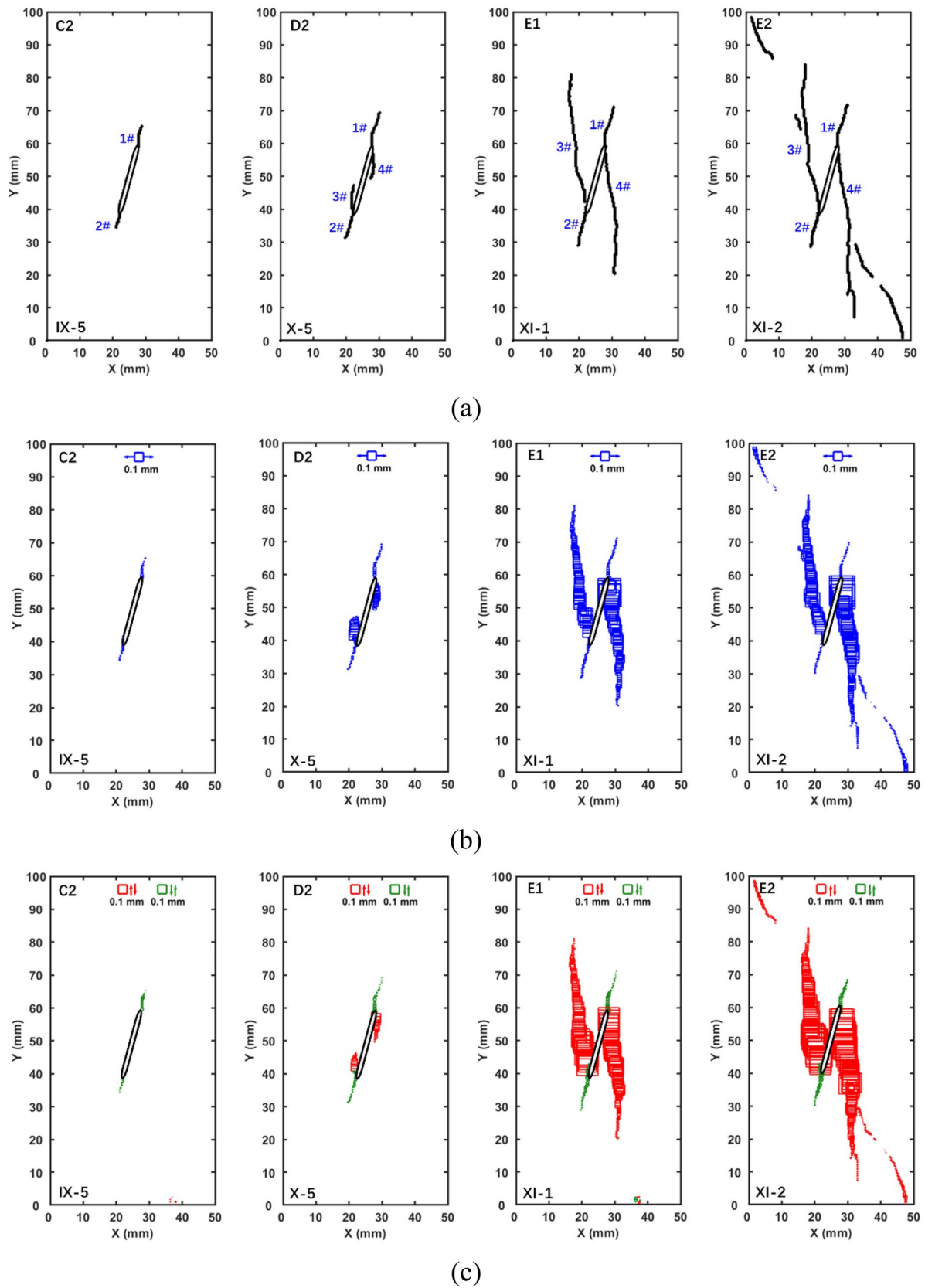
Fig. 15 Crack paths and displacement jumps over initiated cracks in flawed specimen S75-1 at significant time instants: **a** identified crack paths, **b** normal displacement jumps across cracks, and **c** tangential displacement jumps across cracks

level VII, four fan-shaped zones are identified at the flaw tips. In stress level VIII, two high-strain bands appear within the fan-shaped zones (Fig. 12b, D5). The high strain bands extend stably in the first four cycles of stress level IX, but abruptly propagate a long distance in the last cycle, leading to abundant high-amplitude AE events. However, a further increase in stress level and number of cycles does not significantly extend the length of cracks 2# and 3#, but widens the crack openings. The displacement discontinuities across the cracks cause calculation errors in the continuous-based DIC technique, resulting in blank portions along the crack paths (Fig. 12b, F1). The other two fan-shaped strain zones at the flaw tips are also extended until the rock fails. Coplanar cracks, i.e., cracks 4# and 5#, start to nucleate at point F1 and extend under repeated cycles (Fig. 12b, F1–F5). When the specimen is exposed to stress level XI, further extension of crack 4# leads to rock rupture (Fig. 12b, G1). As shown in Fig. 12b, the initiation and propagation of wing cracks are accompanied by few AE events, while the rapid initiation and propagation of secondary cracks are accompanied by dense high-amplitude AE events.

Figure 13 provides additional quantitative information on the cracking behavior and fracture mechanism of the initiated cracks in specimen S45-1. The emergence of the two wing cracks (i.e., crack 1#) is characterized by significant normal displacement jumps and negligible tangential displacement jumps, indicating their tensile nature. On the other hand, cracks 2#, 3#, 4#, and 5# are associated with displacement jumps in both normal and tangential directions, indicating their mixed tensile-shear nature during initiation and propagation.

Figures 14 and 15 provide detailed information on the cracking behaviors and fracture mechanism of the initiated cracks in specimen S75-1 during the stepwise cyclic loading process. The specimen remains in an elastic state until stress level V is applied, and two FPZs appear at the flaw tips (Fig. 14b, A1). The FPZs gradually develop and evolve into cracks 1# and 2# in stress level IX (Fig. 14b, C1, C5). Cracks 3# and 4# appear one after another in the form of high strain bands in stress level X (Fig. 14b, D1, D5) and then abruptly extend a great distance at the 1st cycle of stress level XI (Fig. 14b, E1). The growth rate of these cracks is reflected in the AE distribution in Fig. 14a, where scattered AE events before point E1 indicate limited growth of cracks 1# and 2#. Crack 3# and 4# initiate as anti-wing cracks in stress level X, and a sudden increase in the crack length is observed due to the increase in stress level, accompanied by abundant high-amplitude AE events. The displacement jumps over the initiated cracks in Fig. 15 indicate that all four cracks are mixed tensile-shear cracks, and it is noteworthy that the tensile wing crack is no longer observed in specimen S75-1.

It is important to note that this paper primarily focuses on investigating the behavior of single cracks under stepped cyclic loading, providing valuable insights into their fracturing response. However, in real-world engineering applications, cracks are typically distributed randomly and exhibit a more complex pattern. Therefore, in future research, we aim to optimize the geometry and distribution of cracks in the rock specimens to make them more representative of actual engineering scenarios. This will enable us to better understand the mechanical response of cracked rocks under cyclic loading and provide more applicable insights for engineering practice. Furthermore, although stepwise cyclic loading offers significant advantages in this study, it is important to acknowledge the limitations of simple cyclic loading in fully replicating the characteristics of earthquakes or blasting events. To accurately capture the characteristics of earthquakes or blasting in numerical simulations or laboratory tests, more sophisticated loading models or input approaches should be employed. These advanced models should consider factors such as frequency content, loading rates, and loading histories. Incorporating data from field measurements (Ainalis et al. 2016), recorded ground motions (Xie et al. 2016), or utilizing more specialized testing methodologies (Banadaki 2010) can aid in the development of these advanced models.

Conclusions

To comprehensively understand the fracture mechanism of rocks under repeated loads, a series of stepwise cyclic loading tests were conducted on sandstone specimens containing a single flaw. The damage process and fracture mechanism were quantitatively analyzed by combining DIC and AE techniques. The influence of flaw inclination angle on the mechanical properties and cracking behavior of the rocks was also taken into consideration. The main conclusions can be summarized as follows:

- Repeated loading cycles greatly contribute to the accumulation of damage within rocks, and there is usually a sudden rise in strain energy density as stress level increases. For a given stress level, the total energy density and the dissipated energy density generally decrease with an increasing number of cycles, while the elastic energy density mostly remains constant. The dissipation factor decreases initially and then reaches a constant value as the upper-stress limit increases. Furthermore, rock specimens with smaller inclination angles of flaws tend to exhibit higher dissipation factors.
- Repeated cyclic loading can stimulate the extension of cracks from the flaw tips. Tensile wing cracks initiate at low inclinations and stress levels and become fully developed under stepwise loading, but their initiation and

propagation are inhibited at high flaw inclination angles. Mixed tensile-shear horsetail cracks may experience both stable and unstable crack propagation. Anti-wing cracks tend to rapidly extend to great lengths after initiation without significant stable crack propagation.

- The evolution of AE characteristic parameters can classify crack development during cyclic loading into two stages: stable and accelerated propagation. During the stable crack propagation stage, the AE signals at a specific stress level conform to the Kaiser effect. Additionally, sparsely distributed small-amplitude AE events are observed during the stable stage. However, during the accelerated crack propagation stage, more peaks in the AE count rate and several high-amplitude events are observed compared to the stable crack propagation stage.

Declarations

Conflict of interest The authors declare no competing interests.

References

Ainalis D, Kaufmann O, Tshibangu J-P, Verlinden O, Kouroussis G (2016) Modelling the source of blasting for the numerical simulation of blast-induced ground vibrations: a review. Rock Mech Rock Eng 50:171–193. https://doi.org/10.1007/s00603-016-1101-2

Anderson TL (2017) Fracture mechanics: fundamentals and applications. Fracture Mechanics: Fundamentals and Applications

Banadaki MMD (2010) Stress-wave induced fracture in rock due to explosive action. University of Toronto Toronto

Burdine NT (1963) Rock failure under dynamic loading conditions. Soc Petrol Eng J 3:1–8

Cerfontaine B, Collin F (2017) Cyclic and fatigue behaviour of rock materials: review, interpretation and research perspectives. Rock Mech Rock Eng 51:391–414. https://doi.org/10.1007/s00603-017-1337-5

Duan M, Jiang C, Xing H, Zhang D, Peng K, Zhang W (2020) Study on damage of coal based on permeability and load-unload response ratio under tiered cyclic loading. Arabian J Geosci. https://doi.org/10.1007/s12517-020-5249-4

Geranmayeh Vaneghi R, Thoeni K, Dyskin AV, Sharifzadeh M, Sarmadivaleh M (2020) Strength and damage response of sandstone and granodiorite under different loading conditions of multistage uniaxial cyclic compression. Int J Geomech. https://doi.org/10.1061/(asce)gm.1943-5622.0001801

Haimson BC, Kim CM (1972) Mechanical behaviour of rock under cyclic fatigue

Han Y, Ma H, Yang C, Zhang N, Daemen JJK (2020) A modified creep model for cyclic characterization of rock salt considering the effects of the mean stress, half-amplitude and cycle period. Rock Mech Rock Eng 53:3223–3236. https://doi.org/10.1007/s00603-020-02097-0

Hashash YMA, Hook JJ, Schmidt B, Yao IC (2001) Seismic design and analysis of underground structures. 16:247–293

Karekal S, Hood M (2011) Fracturing mechanism of rock under variable amplitude cyclic loading and implications for design of lightweight rock cutting machines

Lajtai EZ (1971) A theoretical and experimental evaluation of the Griffith theory of brittle fracture. Tectonophysics 11:129–156

Li T, Pei X, Guo J, Meng M, Huang R (2020) An energy-based fatigue damage model for sandstone subjected to cyclic loading. Rock Mech Rock Eng. https://doi.org/10.1007/s00603-020-02209-w

Liu E, He S (2012) Effects of cyclic dynamic loading on the mechanical properties of intact rock samples under confining pressure conditions. Eng Geol 125:81–91. https://doi.org/10.1016/j.enggeo.2011.11.007

Liu XS, Ning JG, Tan YL, Gu QH (2016) Damage constitutive model based on energy dissipation for intact rock subjected to cyclic loading. Int J Rock Mech Min Sci 85:27–32. https://doi.org/10.1016/j.ijrmms.2016.03.003

Liu Y, Dai F, Dong L, Xu N, Feng P (2017) Experimental investigation on the fatigue mechanical properties of intermittently jointed rock models under cyclic uniaxial compression with different loading parameters. Rock Mech Rock Eng 51:47–68. https://doi.org/10.1007/s00603-017-1327-7

Meng Q, Zhang M, Han L, Pu H, Nie T (2016) Effects of acoustic emission and energy evolution of rock specimens under the uniaxial cyclic loading and unloading compression. Rock Mech Rock Eng 49:3873–3886. https://doi.org/10.1007/s00603-016-1077-y

Miao S, Pan P-Z, Konicek P, Yu P, Liu K (2021a) Rock damage and fracturing induced by high static stress and slightly dynamic disturbance with acoustic emission and digital image correlation techniques. J Rock Mech Geotech Eng

Miao S, Pan P-Z, Wu Z, Li S, Zhao S (2018) Fracture analysis of sandstone with a single filled flaw under uniaxial compression. Eng Fract Mech 204:319–343. https://doi.org/10.1016/j.engfracmech.2018.10.009

Miao S, Pan P-Z, Zhao S, Han J, Konicek P (2021b) A new DIC-based method to identify the crack mechanism and applications in fracture analysis of red sandstone containing a single flaw. Rock Mech Rock Eng. https://doi.org/10.1007/s00603-021-02472-5

Momeni A, Karakus M, Khanlari GR, Heidari M (2015) Effects of cyclic loading on the mechanical properties of a granite. Int J Rock Mech Min Sci 77:89–96. https://doi.org/10.1016/j.ijrmms.2015.03.029

Pan P-Z, Miao S, Jiang Q, Wu Z, Shao C (2019) The influence of infilling conditions on flaw surface relative displacement induced cracking behavior in hard rock. Rock Mech Rock Eng. https://doi.org/10.1007/s00603-019-02033-x

Peng K, Wang Y, Zou Q, Liu Z, Mou J (2019a) Effect of crack angles on energy characteristics of sandstones under a complex stress path. Eng Fract Mech. https://doi.org/10.1016/j.engfracmech.2019.106577

Peng K, Zhou J, Zou Q, Yan F (2019b) Deformation characteristics of sandstones during cyclic loading and unloading with varying lower limits of stress under different confining pressures. Int J Fatigue 127:82–100. https://doi.org/10.1016/j.ijfatigue.2019.06.007

Peng K, Zhou J, Zou Q, Zhang J, Wu F (2019c) Effects of stress lower limit during cyclic loading and unloading on deformation characteristics of sandstones. Constr Build Mater 217:202–215. https://doi.org/10.1016/j.conbuildmat.2019.04.183

Ramulu M, Chakraborty AK, Sitharam TG (2009) Damage assessment of basaltic rock mass due to repeated blasting in a railway tunnelling project – a case study. Tunnelling Underground Space Technol 24:208–221. https://doi.org/10.1016/j.tust.2008.08.002

Sorgi C, Gennaro VD (2011) Water-rock interaction mechanisms and ageing processes in chalk. Advances in Data, Methods, Models and Their Applications in Geoscience

Taheri A, Royle A, Yang Z, Zhao Y (2015) Study on variations of peak strength of a sandstone during cyclic loading. Geomech Geophys Geo-Energy Geo-Resour 2:1–10. https://doi.org/10.1007/s40948-015-0017-8

Taheri A, Yfantidis N, Olivares CL, Connelly BJ, Bastian TJ (2016) Experimental study on degradation of mechanical properties of sandstone under different cyclic loadings. Geotech Test J. https://doi.org/10.1520/gtj20150231

Wang Y, Zhou X, Shou Y (2017) The modeling of crack propagation and coalescence in rocks under uniaxial compression using the novel conjugated bond-based peridynamics. Int J Mech Sci 128–129:614–643. https://doi.org/10.1016/j.ijmecsci.2017.05.019

Wong LNY, Einstein HH (2009) Systematic evaluation of cracking behavior in specimens containing single flaws under uniaxial compression. Int J Rock Mech Min Sci 46:239–249. https://doi.org/10.1016/j.ijrmms.2008.03.006

Xiao J-Q, Ding D-X, Jiang F-L, Xu G (2010) Fatigue damage variable and evolution of rock subjected to cyclic loading. Int J Rock Mech Min Sci 47:461–468. https://doi.org/10.1016/j.ijrmms.2009.11.003

Xiao J-Q, Ding D-X, Xu G, Jiang F-L (2009) Inverted S-shaped model for nonlinear fatigue damage of rock. Int J Rock Mech Min Sci 46:643–648. https://doi.org/10.1016/j.ijrmms.2008.11.002

Xie H, Ju Y, Li L (2005) Criteria for strength and structural failure of rocks based on energy dissipation and energy release principles. Chin J Rock Mech Eng 24:3003–3010

Xie H, Peng R, Ju Y (2004) Energy dissipation of rock deformation and fracture. Chin J Rock Mech Eng 23:3565–3570

Xie LX, Lu WB, Zhang QB, Jiang QH, Wang GH, Zhao J (2016) Damage evolution mechanisms of rock in deep tunnels induced by cut blasting. Tunnelling Underground Space Technol 58:257–270. https://doi.org/10.1016/j.tust.2016.06.004

Yang F, Hu D, Zhou H, Lu J (2020a) Physico-mechanical behaviors of granite under coupled static and dynamic cyclic loadings. Rock Mech Rock Eng 53:2157–2173. https://doi.org/10.1007/s00603-019-02040-y

Yang S-Q, Huang Y-H, Tang J-Z (2020b) Mechanical, acoustic, and fracture behaviors of yellow sandstone specimens under triaxial monotonic and cyclic loading. Int J Rock Mech Min Sci. https://doi.org/10.1016/j.ijrmms.2020.104268

Zang A et al (2021) Relaxation damage control via fatigue-hydraulic fracturing in granitic rock as inferred from laboratory-, mine-, and field-scale experiments. Sci Rep. https://doi.org/10.1038/s41598-021-86094-5

Zhang S, Lai Y, Zhang X, Pu Y, Yu W (2004) Study on the damage propagation of surrounding rock from a cold-region tunnel under freeze–thaw cycle condition. Tunn Undergr Space Technol 19:295–302

Zhang Z (2016) Rock fracture and blasting: theory and applications. B-H/Elsevier Science, Oxford, p 2015

Zhao K et al (2021) Damage evaluation of rock salt under multilevel cyclic loading with constant stress intervals using AE monitoring and CT scanning. J Petrol Sci Eng. https://doi.org/10.1016/j.petrol.2021.109517

Zheng Q, Liu E, Yu D, Liu M (2020) Fatigue and damage properties of non-consecutive jointed mudstone samples subjected to cyclic triaxial loading. Bull Eng Geol Environ 79:2467–2481. https://doi.org/10.1007/s10064-019-01693-x

Zhu X-Y, Chen X-D, Dai F (2020) Mechanical properties and acoustic emission characteristics of the bedrock of a hydropower station under cyclic triaxial loading. Rock Mech Rock Eng. https://doi.org/10.1007/s00603-020-02218-9

Zhu Z, Mohanty B, Xie H (2007) Numerical investigation of blasting-induced crack initiation and propagation in rocks. Int J Rock Mech Min Sci 44:412–424. https://doi.org/10.1016/j.ijrmms.2006.09.002